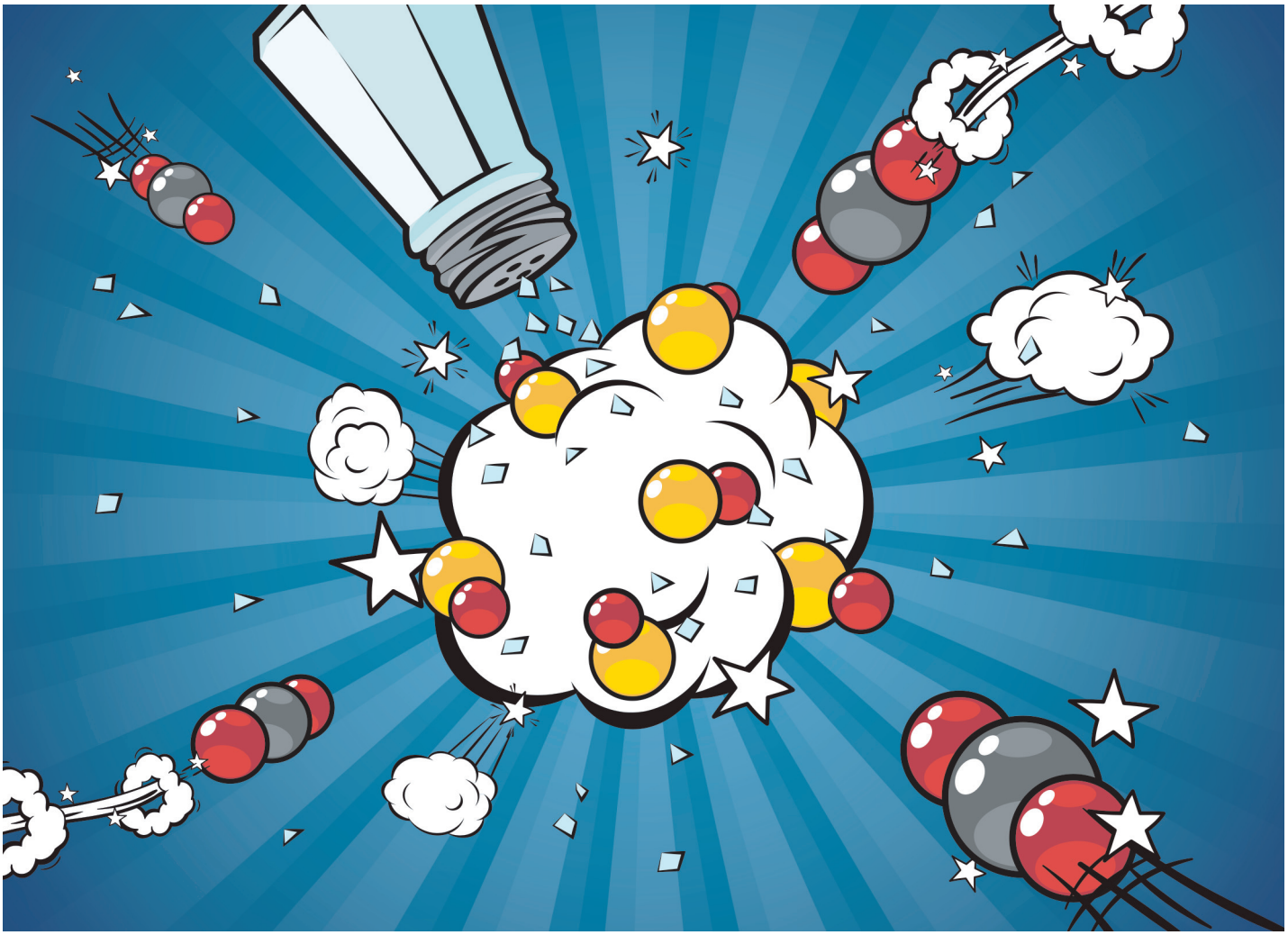

Showcasing research from the Laboratory of Energy Science and Engineering (LESE) at ETH Zürich, Switzerland.

Effect of molten sodium nitrate on the decomposition pathways of hydrated magnesium hydroxycarbonate to magnesium oxide probed by *in situ* total scattering

Synchrotron Pair Distribution Function analysis provided an atomic level picture of the role of molten salts on the mechanisms of MgO formation from a hydrated magnesium carbonate. Without molten salts, MgO is formed through an amorphous magnesium carbonate intermediate. Molten $NaNO_3$ promotes the rapid release of H_2O and CO_2 molecules from the hydrated magnesium carbonate structure and enhances the crystallization of both the $MgCO_3$ intermediate and the MgO product. MgO promoted by $NaNO_3$ captures CO_2 at a significantly enhanced rate.

As featured in:

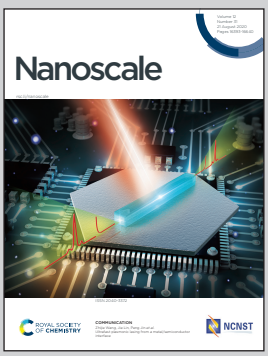

See Paula M. Abdala, Christoph R. Müller *et al.*, *Nanoscale*, 2020, **12**, 16462.

ROYAL SOCIETY OF CHEMISTRY

rsc.li/nanoscale

Registered charity number: 207890

Nanoscale

PAPER

View Article Online
View Journal | View Issue

Cite this: *Nanoscale*, 2020, **12**, 16462

Effect of molten sodium nitrate on the decomposition pathways of hydrated magnesium hydroxycarbonate to magnesium oxide probed by *in situ* total scattering†

Margarita Rekhtina, [a] Alessandro Dal Pozzo, [a,b] Dragos Stoian,[c] Andac Armutlulu, [a] Felix Donat, [a] Maria V. Blanco,[c] Zhu-Jun Wang, [d] Marc-Georg Willinger, [d] Alexey Fedorov, [a] Paula M. Abdala *[a] and Christoph R. Müller *[a]

The effect of $NaNO_3$ and its physical state on the thermal decomposition pathways of hydrated magnesium hydroxycarbonate (hydromagnesite, HM) towards MgO was examined by *in situ* total scattering. Pair distribution function (PDF) analysis of these data allowed us to probe the structural evolution of pristine and $NaNO_3$-promoted HM. A multivariate curve resolution alternating least squares (MCR-ALS) analysis identified the intermediate phases and their evolution upon the decomposition of both precursors to MgO. The total scattering results are discussed in relation with thermogravimetric measurements coupled with off-gas analysis. MgO is obtained from pristine HM (N_2, 10 °C min^{-1}) through an amorphous magnesium carbonate intermediate (AMC), formed after the partial removal of water of crystallization from HM. The decomposition continues *via* a gradual release of water (due to dehydration and dehydroxylation) and, in the last step, *via* decarbonation, leading to crystalline MgO. The presence of molten $NaNO_3$ alters the decomposition pathways of HM, proceeding now through AMC and crystalline $MgCO_3$. These results demonstrate that molten $NaNO_3$ facilitates the release of water (from both water of crystallization and through dehydroxylation) and decarbonation, and promotes the crystallization of $MgCO_3$ and MgO in comparison to pristine HM. MgO formed from the pristine HM precursor shows a smaller average crystallite size than $NaNO_3$-promoted HM and preserves the initial nano-plate-like morphology of HM. $NaNO_3$-promoted HM was decomposed to MgO that is characterized by a larger average crystallite size and irregular morphology. Additionally, *in situ* SEM allowed visualization of the morphological evolution of HM promoted with $NaNO_3$ at a micrometre scale.

Received 1st March 2020,
Accepted 26th May 2020

DOI: 10.1039/d0nr01760d

rsc.li/nanoscale

Introduction

The development of efficient solid sorbents for CO_2 capture plays a key role in carbon capture storage and utilization (CCSU) technologies, which are considered strategic in reducing greenhouse emissions and mitigating global warming.[1–4]

MgO-based materials are attractive CO_2 sorbents for operation at moderate temperatures (200–450 °C)[5] due to their high theoretical capture capacity of 1.09 g CO_2 per g MgO[6] and for being economically promising,[7] environmentally benign and naturally abundant.[8] Despite these advantages, the application of MgO as a CO_2 sorbent has been hampered by its slow carbonation kinetics. In recent years, a breakthrough in the development of effective MgO-based sorbents has been achieved through their promotion by molten salts.[9] The presence of molten alkali metal nitrates (such as $LiNO_3$, $NaNO_3$, KNO_3 and mixtures thereof) drastically accelerates the rate of MgO carbonation;[10–17] however, an in-depth understanding of the role of molten salts in the carbonation of MgO has yet to be obtained. It has been proposed that molten salts act as a phase transfer catalyst in the reaction between MgO and CO_2.[16] The dissolution of MgO in the molten salt, leading to the formation of solvated Mg–O pairs, may help to overcome

[a]*Laboratory of Energy Science and Engineering, Department of Mechanical and Process Engineering, ETH Zürich, Leonhardstrasse 21, 8092 Zürich, Switzerland. E-mail: abdalap@ethz.ch, muelchri@ethz.ch*
[b]*Laboratory of Industrial Safety and Environmental Sustainability, Department of Civil, Chemical, Environmental and Materials Engineering, Alma Mater Studiorum–Università di Bologna, Via Terracini 28, 40131 Bologna, Italy*
[c]*European Synchrotron Radiation Facility, 71 Avenue des Martyrs, Grenoble, France*
[d]*Scientific Center for Optical and Electron Microscopy, ETH Zürich, Auguste-Piccard-Hof 1, 8093 Zurich, Switzerland*

†Electronic supplementary information (ESI) available. See DOI: 10.1039/d0nr01760d

the large lattice enthalpy of crystalline MgO and thereby facilitate carbonation. The solvated pairs can react with CO_2 adsorbed on the MgO surface at the triple phase boundaries between solid, gaseous and the molten phases. Other studies have postulated that the molten alkali metal nitrates act primarily as a diffusion medium for CO_2, preventing the formation of a CO_2-impermeable unidentate carbonate and promote the rapid generation of carbonate ions.[17] Elucidation of the mechanism behind the promoting effect of molten salts on the CO_2 capture of MgO is key for the rational design of more effective MgO-based CO_2 sorbents.

In addition to the accelerated carbonation of MgO, the presence of molten salts promotes also the decomposition of magnesium carbonate (regeneration of the CO_2 sorbent) and hydrated magnesium hydroxycarbonates.[16–19] For example, based on thermogravimetric analysis (TGA) the decomposition temperature of $MgCO_3$ mixed with $NaNO_3$ was determined to be lowered by 50 °C with respect to un-promoted $MgCO_3$.[16] Similarly, it was observed that the presence of alkali nitrates also affects the decomposition of hydromagnesite, $Mg_5(CO_3)_4(OH)_2{\cdot}4H_2O$ (HM).[11]

HM is a naturally occurring form of magnesium carbonate[20] and is widely employed as a precursor for the synthesis of MgO-based sorbents.[11,16,19,21] Upon thermal treatment, HM decomposes *via* the loss of water of crystallization, dehydroxylation and decarbonation, leading ultimately to the formation of crystalline MgO.[22–24] The overall decomposition process involves amorphous intermediate phases, yet, their structure, *i.e.*, the local atomic arrangement of the intermediates, is still unknown.[25–27] Previous TGA-based experiments[11,19] have shown a decrease in the decomposition temperature of HM in the presence of $NaNO_3$. The crystallite size of the resulting MgO, obtained in the presence of molten nitrates, was also larger than that of the decomposition of unpromoted HM.[11] It was suggested that $NaNO_3$ in its molten state facilitates the release of CO_2.[19] However, there is limited understanding of the effect of $NaNO_3$ and its physical state during the formation of MgO from HM.

Key tools to understand in more detail the effect of alkali salt promoters on the decomposition of $MgCO_3$ and HM and the carbonation of MgO, are *in situ* studies. In this regard, the pair distribution function (PDF) analysis of total scattering data is of great interest as it provides information about both crystalline and amorphous intermediates.[28,29] PDF analysis is based on high-energy X-rays, which allows for high penetration depth in versatile sample environments including reaction cells, rendering it ideal for *in situ* studies. Interrogation of materials consisting of solely light elements by PDF is particularly advantageous[30,31] when compared to other techniques for probing the local-structure such as X-ray absorption spectroscopy (XAS) that requires high vacuum and a tailored cell owing to the tender X-ray energy of the absorption edges of Mg and Na.[32,33] Advancements in time-resolved *in situ* and *operando* PDF analysis are, therefore, of great importance in the understanding and development of more active and stable MgO-based CO_2 sorbents.

This work focuses on determining the role of $NaNO_3$ on the decomposition pathways of HM leading to the formation of MgO and the physical state of $NaNO_3$ (and changes thereof) during this process. To this end, *in situ* X-ray total scattering studies during the thermal treatment of pristine HM and $NaNO_3$-promoted HM were carried out. Bulk $NaNO_3$ was also investigated to determine the evolution of its structure when transitioning from the crystalline to the molten state. The analysis of the *in situ* total scattering data by the PDF technique, assisted by the multivariate curve resolution alternating least squares (MCR-ALS) method, provided information on the structural evolution in the local and medium-range order during the decomposition of HM. $NaNO_3$ influences this transformation not only by accelerating dehydration, dehydroxylation and decarbonation of HM, but also by promoting crystallization of $MgCO_3$ and MgO.

Experimental

Materials

Hydromagnesite ($Mg_5(CO_3)_4(OH)_2{\cdot}4H_2O$, Acros Organics, extra pure) and sodium nitrate ($NaNO_3$, Sigma-Aldrich, ≥99.5%) were used as received. HM-20$NaNO_3$ (with a Na : Mg molar ratio of 20 : 100) was obtained by a wet mixing method, as reported elsewhere.[11] $Mg_5(CO_3)_4(OH)_2{\cdot}4H_2O$ and $NaNO_3$ were mixed in deionized water and stirred magnetically for 1 h at room temperature. The aqueous slurry was dried at 120 °C for 12 h and ground to a fine powder in an agate mortar.

TGA and heat flow measurements coupled with gas analysis

TGA and heat flow (HF) measurements (Mettler Toledo TGA/DSC3) were performed using *ca.* 70 mg of the specimen loaded into an alumina crucible (900 μl) and heated from 25 to 600 °C under a flow of nitrogen (80 mL min^{-1}, measured and controlled at normal temperature and pressure, NTP) at a heating rate of 10 °C min^{-1}. The rate of mass loss was calculated as the first derivative of the normalized weight loss with respect to time. An ABB EL3020 FTIR gas analyser and a Sensirion SHT31 humidity sensor were connected to the outlet of the TGA to measure the mole fractions of CO_2 and H_2O, respectively, in the off-gas stream. Integrating the mole fractions of CO_2 and H_2O over time and multiplying them by the molar flow rate of the gas yielded the total amounts of CO_2 and H_2O that evolved from the sample.

In situ X-ray total scattering

In situ total scattering measurements were performed at the ID31 beamline at the European Synchrotron Radiation Facility (ESRF) in Grenoble, France. The incident X-rays were set to an energy of 70.0 keV (λ = 0.1771 Å) and were focused to a size of 0.6 mm × 0.6 mm. The data were collected using a 16-inch PerkinElmer 1621 2D detector. The sample-to-detector distance was set to *ca.* 26 cm to collect total scattering data $I(Q)_{26}$; to acquire more resolved scattering patterns $I(2\theta)_{83}$ sample-to-detector distance was changed to *ca.* 83 cm (Fig. S2†). The

materials were loaded in a quartz capillary reactor[34] (external diameter = 1 mm, wall thickness = 0.01 mm), heated *via* an air blower. A temperature calibration was carried out first with a thermocouple placed inside the sample bed to determine the actual sample temperature as a function of the air blower temperature (the procedure was repeated twice to verify the reproducibility). The total scattering data were collected every 120 s using an exposure time of 10 s per acquisition while ramping up in the N_2 flow (10 °C min^{-1}, 5 mL min^{-1}), more detailed scheme of data acquisition can be found in Fig. S2 and S3.† A CeO_2 diffraction standard (National Institute of Standards and Technology, NIST) was used to determine the azimuthal parameters and the sample-to-detector distances. Azimuthal integration and normalization on the incident beam intensity were done using the pyFAI software package.[35] The PDFGetX3 software package was used to subtract the background signal from an empty capillary (r_{poly} = 1.15 Å) and to obtain the coherent scattering function $I(Q)$, reduced total scattering structure function $F(Q)$ and the reduced pair distribution function $G(r)$.[36] The total scattering data were analysed up to Q_{max} = 22 $Å^{-1}$ (Q = scattering vector). The PDF data of the CeO_2 diffraction standard was used to determine the damping and broadening parameters of the PDF peaks due to the experimental resolution (Q_{damp} = 0.045 $Å^{-1}$; Q_{broad} = 0.026 $Å^{-1}$, Fig. S20†). These parameters were then fixed during the PDF refinements that were carried out with PDFgui[37] using previously published structures from the Inorganic Crystal Structure Database (ICSD) database. Rietveld refinements of the XRD data ($I(2\theta)_{83}$) were carried out using FullProf software.[38] Line broadening analysis was implemented in the Rietveld analysis; the instrumental resolution function was determined from the refinement of CeO_2 reference (NIST). Additional information can be found in ESI.†

MCR-ALS analysis was employed as a data reduction tool for the analysis of *in situ*, time-resolved PDF data obtained during the thermal treatment of HM and HM-20$NaNO_3$ under N_2. The MCR-ALS scripts, written in Matlab®, were used in the present work.[39] MCR-ALS analysis was carried out in the r-range (r = interatomic distances) from 0 to 7 Å; the number of components used in the analysis was estimated based on a principal component analysis and prior knowledge of the systems. A more detailed description of the MCR-ALS analysis and deconvolution procedure can be found in the ESI.†

In situ scanning electron microscopy (SEM)

In situ SEM experiments were performed inside the chamber of a modified commercial ESEM (Thermo Scientific™ Quattro S). The vacuum system of the ESEM was modified and upgraded with oil-free prevacuum pumps. The instrument is equipped with a homemade laser heating stage, a gas supply unit (mass flow controllers from Bronkhorst), and a mass spectrometer (Pfeiffer OmniStar) for the analysis of the chamber atmosphere. After each sample loading, the chamber was pumped out to around 10^{-3} Pa, purged with pure nitrogen, and pumped again to 10^{-3} Pa successively for several times. The temperature was measured *via* a K-type thermocouple that was spot-welded onto the sample supporting substrate. *In situ* observation was performed at temperatures ranging from room temperature to 450 °C, with 46 Pa N_2 (99.9995% purity). During the experiments, the microscope was operated at an acceleration voltage of 7.5 kV. Images were recorded by a large field detector. No influence of the electron beam on the sample could be observed during annealing process. The imaged regions and their respective surroundings showed similar behaviour, as evidenced by changing the magnification or by moving the sample under the beam. Furthermore, no electron beam induced contamination was observed.

Transmission electron microscopy (TEM)

The morphology of the materials was studied by TEM (FEI Talos F200X) and HAADF-STEM (high-angle annular dark field – canning transmission electron microscope) equipped with a high-brightness field-emission gun, a HAADF detector, and a large collection-angle energy-dispersive X-ray spectroscopy (EDX) detector. The operation voltage of the instrument was set to 200 kV. The powders were dispersed onto Cu grids coated with lacey carbon.

Results and discussion

First, we investigated the decomposition of the HM and HM-20$NaNO_3$ materials using thermal gravimetric analysis with simultaneous heat flow (HF) measurements, coupled with the analysis of the off-gases (H_2O, CO_2). Additionally, *in situ* PDF analysis of the structural evolution of HM and HM-20$NaNO_3$, as well as the reference $NaNO_3$ during thermal treatment, allowed us to probe the decomposition pathways. Finally, the structural and morphological characteristics of the MgO produced from both precursors were determined by *in situ* XRD, PDF, SEM and *ex situ* HAADF-STEM.

TGA/HF coupled gas analysis

Thermolysis of HM and HM-20$NaNO_3$ in N_2 was studied by TGA allowing the determination of changes in the sample mass (Fig. 1a and b) and the HF (Fig. 1c). The concentrations of H_2O and CO_2 in the off-gas were measured simultaneously by a humidity sensor and a FTIR gas analyser (Fig. 1d and e).

The differential change of the mass of HM exhibits two main peaks at 270 °C and 475 °C (Fig. 1b, blue trace), corresponding to two exothermic minima in the HF data (Fig. 1c, blue trace). The first peak corresponds to the release of water of crystallization (eqn (1)), according to the simultaneous analysis of the H_2O released in the off-gas stream (Fig. 1d, blue trace). The long tailing of the H_2O peak at higher temperatures, showing a continuous and gradual release of H_2O between 270 and 500 °C, can be ascribed to the dehydroxylation of HM (eqn (2)). The second peak centred at 475 °C in the differential mass change curve is due to the release of CO_2 through the decomposition of the carbonates (eqn (3)). This decomposition proceeds between 350–550 °C (Fig. 1e, blue

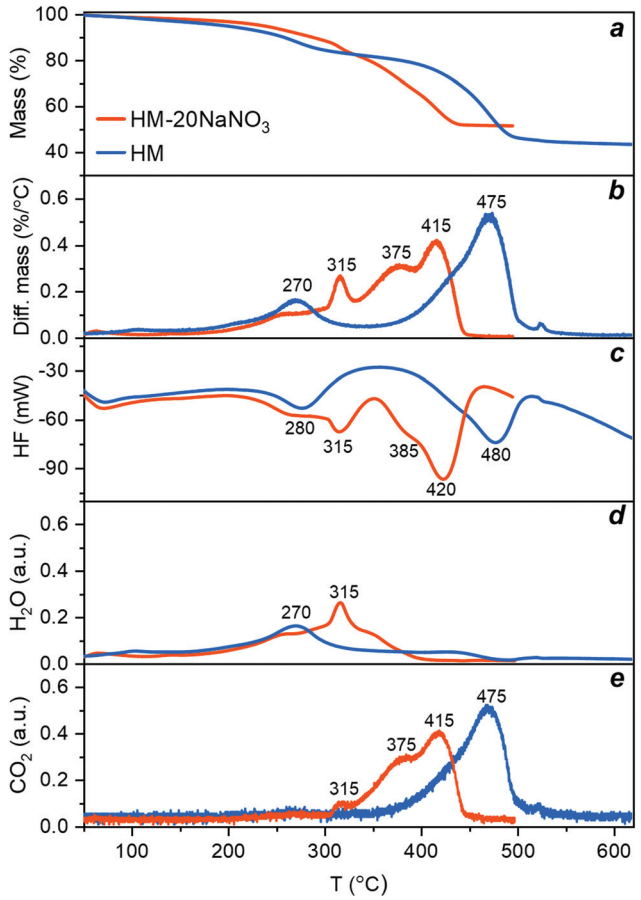

Fig. 1 Thermal decomposition of HM (blue) and HM-20$NaNO_3$ (red) during thermal treatment in N_2 (10 °C min^{-1}): (a) mass loss and (b) rate of mass loss determined by TGA; (c) heat flow and simultaneous measurement of (d) H_2O and (e) CO_2 released during the reaction.

trace). Table S1† summarizes the observed mass losses. The values obtained are in line with the following decomposition pathway of HM:[23,26]

$$Mg_5(CO_3)_4(OH)_2 \cdot 4H_2O \rightarrow Mg_4(CO_3)_4 \cdot Mg(OH)_2 + 4H_2O \quad (1)$$

$$Mg_4(CO_3)_4 \cdot Mg(OH)_2 \rightarrow 4MgCO_3 + MgO + H_2O \quad (2)$$

$$MgCO_3 \rightarrow MgO + CO_2 \quad (3)$$

Turning now to HM promoted by $NaNO_3$, we observe that the presence of $NaNO_3$ significantly alters the decomposition profile of HM, as observed in both the differential mass change and HF profiles (Fig. 1b and c, red trace). The decomposition of HM-20$NaNO_3$ was completed at 450 °C, *i.e.* 100 °C lower than for HM. In addition, the number of peaks increased. For HM-20$NaNO_3$, the initial mass loss at *ca.* 260 °C, *i.e.*, the release of water of crystallization, was not affected significantly by the presence of $NaNO_3$. $NaNO_3$ is still crystalline at this temperature (see section below and Fig. S1 and S4†). A more pronounced, and rather sudden release of water between 300 and 335 °C (with a maximum at 315 °C) correlates with the melting of $NaNO_3$, as indicated by the HF signal of this sample and the reference experiment using pure $NaNO_3$ (Fig. S1 and S4†). The dehydroxylation of HM is completed at 400 °C, *i.e.*, 100 °C lower than for HM. Similarly, previous TGA and XRD studies have shown that the dehydroxylation of the brucite phase, $Mg(OH)_2$, was facilitated by the presence of $NaNO_3$.[40] Therefore, these results suggest that the molten salt acts as a phase-transfer agent that facilitates the migration of H_2O from HM into the gas phase, possibly due to the dissolution (solvation) of H_2O in the melt. The subsequent release of CO_2 splits into two main peaks centred at 375 °C and 415 °C (Fig. 1e) which are, respectively, 100 °C and 60 °C lower than the single peak observed for HM. We speculate that this splitting is related to different decomposition intermediates, which can be evidenced by *in situ* PDF studies (*vide infra*). Overall, these results indicate that (molten) $NaNO_3$ facilitates the release of water of crystallization, dehydroxylation and the decomposition of the carbonates.

In situ PDF and XRD analyses

The structural changes occurring in HM and HM-20$NaNO_3$ during the thermal heat treatment in N_2 were also followed by PDF and XRD. However, the overlapping signals of the different phases in the PDF of HM-20$NaNO_3$, make the identification of the dynamic phase changes in this material challenging. Therefore, an additional *in situ* experiment using pure $NaNO_3$ and heating it from 40 °C to its melting point was performed as a reference.

Phase transitions in $NaNO_3$. The *in situ* PDFs, $G(r)$, of $NaNO_3$ when heated from 40 °C to 308 °C in N_2 are presented in Fig. 2a, while the corresponding XRD patterns are plotted in Fig. S4.† At room temperature $NaNO_3$ exhibits a calcite-type structure ($R\bar{3}c$ space group, illustrated in Fig. 2b).[41] The PDF of pristine $NaNO_3$ at the lowest acquired temperature (*ca.* 40 °C) showed intense correlations in both the short ($1 < r < 5$ Å) and the medium r-ranges ($5 < r < 25$ Å), as expected for a crystalline material. According to the simulated PDF for $NaNO_3$, the peaks in the short r-range, *i.e.,* those centred at 1.25 Å and 2.20 Å, correspond to the, respectively, N–O and O–O intramolecular correlations of the NO_3^- group (Fig. S5†). The peaks at 2.46 Å and 3.32 Å are due to intermolecular pairs: the former corresponds to Na–O and the latter to the overlapping correlations of Na–N, Na–O and O–O. Upon heating to 290 °C, $NaNO_3$ undergoes a second-order (order-disorder) phase transition, from an $R\bar{3}c$ to an $R\bar{3}m$ space group (marked by a gradual disappearance of the superstructure (113) reflection in the diffraction patterns, Fig. S4†),[42–44] associated with an increase of the orientational freedom of nitrate groups. This transition appears as a gradual decrease in intensity of the intermolecular O–O and Na–O correlations in the short r-range of the PDF (*i.e.*, an increasing disorder between the NO_3^- groups). In addition, the PDF data in Fig. 2a provide a direct evidence for the evolution of the Na–O distance, *i.e.*, a continuous increase from 2.46 Å to 2.47 Å between 40 °C and 240 °C, followed by a sharper increase from 2.47 Å to 2.49 Å between 255 °C and 290 °C (Fig. S6†). The N–O distance remained largely unchanged during this order-disorder transformation

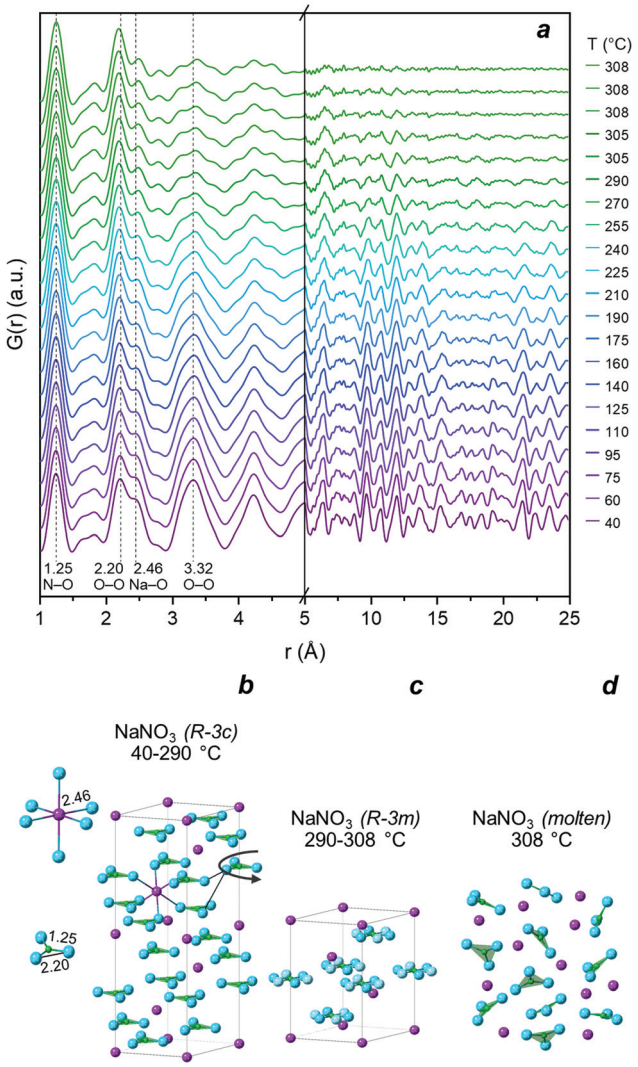

Fig. 2 (a) PDF of $NaNO_3$ heated from 40 °C to 308 °C in N_2 and hold at 308 °C for 10 min; (b) illustration of the $NaNO_3$ $R\bar{3}c$ (ICSD: 180912) crystalline structure and short-range correlations below 2.5 Å; (c) $R\bar{3}m$ (ICSD: 180920) crystalline structure; (d) schematic representation of the molten $NaNO_3$ state. Color legend: blue – oxygen, purple – sodium, green – nitrogen.

(variations < 0.006 Å), evidencing the rigid structure of the NO_3^- group. The extent of the variations in the N–O distance during the second order phase transition has been a matter of debate in the literature.[41,42] However, previous studies have determined the interatomic distances from XRD analysis and, therefore, they depend on the structural model used.[41,42] Here, the PDF analysis provides direct information in real space, confirming that the N–O distance remains largely unchanged while the disorder between the nitrate groups increases gradually. When reaching 308 °C, the long-range ordering decreased, associated with vanishing correlations for $r > 5$ Å, which is in line with the melting (solid–liquid) transition of $NaNO_3$. The melting of $NaNO_3$ at 308 °C is supported by XRD analysis, showing the disappearance of all Bragg peaks due to $NaNO_3$ (Fig. S4†). The PDF of pure, molten $NaNO_3$ (*i.e.*, the final measurement at 308 °C in Fig. 2a) shows peaks due to intramolecular N–O and O–O (1.25 Å and 2.20 Å) pairs, and weaker signals due to intermolecular correlations at 2.49 Å(Na–O) and between 2.5–5 Å (Na–Na, Na–N, Na–O, N–N, N–O, O–O).[45] No correlations above 5 Å were present due to the lack of long-range order in molten salts.[46,47]

Structural evolution of HM and HM-20NaNO$_3$. The PDFs collected during the decomposition of HM under thermal treatment in N_2 from 40 °C to 475 °C are presented in Fig. 3a. At 40 °C, the shortest correlation in the PDF of HM is at 1.27 Å and is assigned to the C–O intramolecular distances in the CO_3^{2-} group. The peak at 2.12 Å corresponds to the first intermolecular correlation Mg–O in the HM structure. The crystal structure of HM is described by a monoclinic arrangement ($P2_1/c$, Fig. S7†)[48] with three different crystallographic Mg sites in a distorted octahedral environment, coordinated to oxygen of the carbonate, hydroxyl groups or water molecules.[48,49] The corresponding simulated PDF and partial PDFs are shown in Fig. S8a.†

Above 190 °C, the disappearing correlations for $r > 5$ Å in HM reveal the loss of long-range order (*i.e.*, amorphization), which coincides with the release of water of crystallization (based on the TGA results, Fig. 1d).

The gradual removal of bound water from the structure disrupts the hydrogen bonding network between water molecules,[48,50] leading to an amorphous (partially hydrated and hydroxylated) magnesium carbonate (AMC). The material remains amorphous during the continuous loss of water of crystallization and dehydroxylation. Indeed, the intensity of the peak at *ca.* 3.0 Å (mainly ascribed to O–O distance between H_2O molecules and between H_2O and CO_3^{2-} in the HM structure) decreased gradually. The loss of water was accompanied by a gradual change in the local structure, with notably, the Mg–O correlation (initially at *ca.* 2.12 Å) evolving towards a more asymmetric peak (inset in Fig. S9a and c†) and shifting ultimately towards a higher r (*ca.* 2.15 Å) and forming a shoulder at $r < 2.0$ Å. Between 350–450 °C, *i.e.*, in the dehydroxylation temperature range (Fig. 1d), the splitting of the Mg–O peak in AMC intensified. This shows that during the dehydration and dehydroxylation of AMC, the distribution of the Mg–O distances becomes broader compared to HM. A similar behaviour for the first Ca–O coordination sphere upon release of water has been observed previously in the case of amorphous calcium carbonate (ACC).[30] This observation can probably be linked to a re-arrangement of carbonate ions, compensating for the loss of water and hydroxyl groups around Mg, as has been shown previously for ACC by PDF and empirical potential structural refinement (EPSR) studies.[51,52]

The onset of MgO crystallization occurred at *ca.* 450 °C, marked by the growth of a Mg–O and Mg–Mg correlation at 2.11 Å and 2.98 Å that are characteristic for cubic MgO. Furthermore, the appearance of correlations for $r > 5$ Å indicates a long-range order in the MgO formed. The formation of a peak centered at 2.11 Å (and the decrease of the shoulder at *ca.* 1.5–2 Å) agrees with the formation of Mg–O octahedra within cubic MgO. Some degree of structural disorder seems

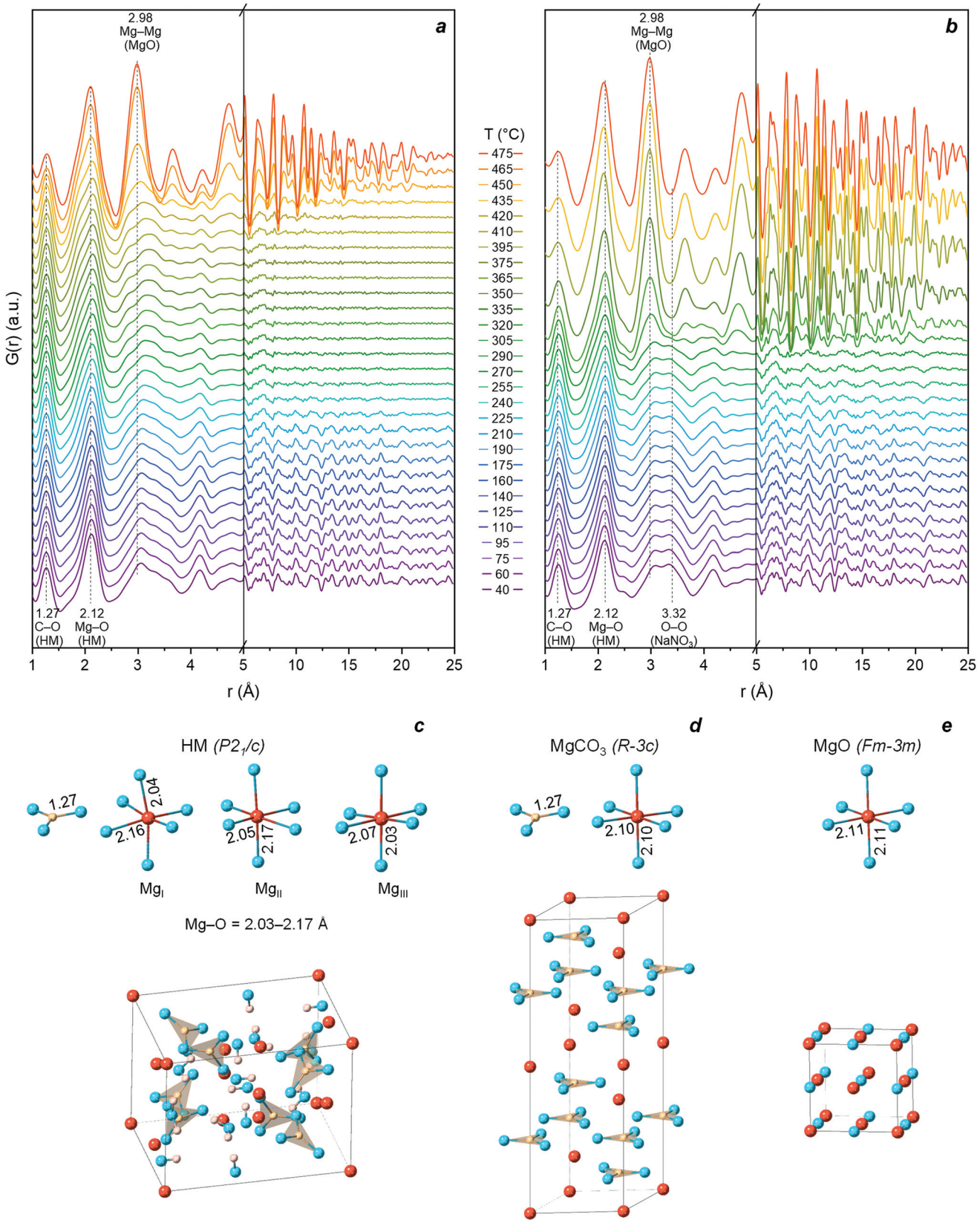

Fig. 3 PDF obtained while heating (a) HM and (b) HM-20$NaNO_3$ from 40 °C to 475 °C in N_2. Illustration of the crystal structure and short-range correlations below 2.5 Å of (c) HM ($P2_1/c$, ICSD: 920); (d) crystalline-$MgCO_3$ ($R\bar{3}c$, ICSD: 40117); (e) MgO ($Fm\bar{3}m$, ICSD: 9863). Color legend: blue – oxygen, red – magnesium, pink – hydrogen, yellow – carbon.

to remain in MgO (see further characterization in the following section). Further crystal growth of MgO occurred upon heating to 475 °C, as confirmed by the intensification of correlations for $r > 5$ Å (cut-off point *ca.* 25 Å at 475 °C). In parallel to occurrence of the Mg–O and Mg–Mg peaks arising from crystalline MgO, the intensity of the peak attributed to C–O of the CO_3^{2-} group (according to the crystallographic model of HM, Fig. S8†) decreased due to the decomposition of the carbonate to the corresponding oxide (Fig. S9c and d†). However, the low *r*-range of the PDF data is affected by the truncation effect using a finite *Q*-range, resulting in termination ripples.[53] Therefore, even after the complete decomposition of the carbonate there is still a small peak at r of approximately 1.27 Å (the intensity of the low-*r* peaks as a function of temperature are shown in Fig. S10a and b†). A confirmation of these qualitative observations is given further below when using MCR-ALS analysis to obtain a quantitative assessment of the phase evolution with temperature.

Turning now to HM-20$NaNO_3$ (Fig. 3b), at the initial temperature (40 °C) it consists of a mixture of crystalline HM and $NaNO_3$. The atomic correlations of $NaNO_3$ overlapped with those of HM and the latter dominated the PDF signal; however, the prominent peak at *ca.* 3.32 Å can be assigned to crystalline $NaNO_3$. As in the case of pristine HM, during the release of water of crystallization, amorphization and a splitting of the Mg–O distance was observed (Fig. S9b and d†). Reaching 305 °C, intense atomic correlations that are assigned to both crystalline-$MgCO_3$ and MgO appeared in the PDF data (Fig. S11 and S13†). The formation of MgO and $MgCO_3$ atomic correlations is confirmed by the appearance of diffraction peaks in the XRD data (Fig. S11†). Importantly, the formation of crystalline phases occurs simultaneously with the melting of $NaNO_3$ (confirmed by XRD in Fig. S4†), demonstrating that molten $NaNO_3$ changed the crystallization behaviour of MgO and $MgCO_3$ from HM.

Subsequently, we performed MCR-ALS analysis of the *in situ* PDF data to compare quantitatively the structural evolution of HM and HM-20$NaNO_3$ upon their thermal decomposition. MCR-ALS allows to resolve the compositional changes of complex mixtures without requiring references or structural information. Using MCR-ALS analysis, a complex system with multiple evolving components is reduced to the least number of components that can describe the initial dataset. This makes MCR-ALS especially suitable for the analysis of large datasets generated during *in situ* and/or *operando* experiments, *e.g.*, IR,[54] Raman,[55] XAS,[56] XRD,[57] or PDF.[58,59] MCR-ALS provides the characteristic profiles of the individual components and the evolution of these components with time (time-concentration profiles).[59] Comprehensive overviews on MCR-ALS analysis can be found in the literature[39,60] and ESI† section.

The evolution of HM upon thermal treatment in N_2 is well described by three components, as determined by MCR-ALS (Fig. 4a). Importantly, the components obtained by MCR-ALS analysis have a physical meaning (Fig. S13†), enabling their identification by comparison with references. We could assign the three components predicted by MCR-ALS as C1 = HM, C2 = AMC and C3 = MgO. The evolution of these components is plotted in Fig. 4a. A significant fraction of AMC appeared at *ca.* 200 °C and coincided with an appreciable release of water of crystallization from the HM structure (Fig. 1d). The final transformation of AMC to MgO started at 450 °C and was completed at 475 °C. Hence, the PDF experiment revealed that the thermal decomposition of HM to MgO proceeded through an AMC intermediate that formed during the continuous loss of water of crystallization.

According to MCR-ALS analysis, the decomposition of HM-20$NaNO_3$ can be described by four components, confirming an alteration of the decomposition pathway in the presence of (molten) $NaNO_3$. These four components extracted

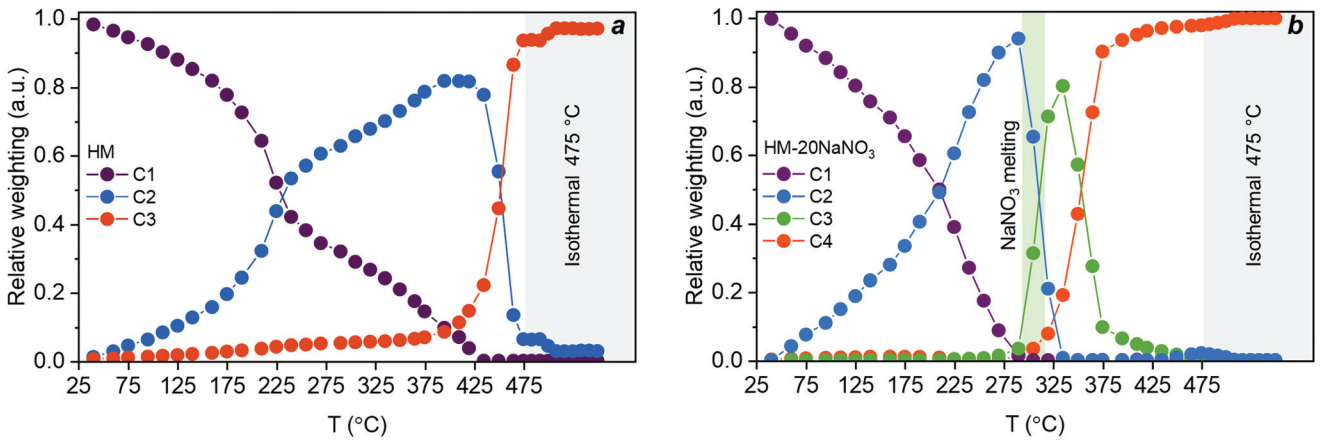

Fig. 4 Concentration profiles extracted by MCR-ALS analysis for (a) the decomposition of HM with components assigned to HM (C1), AMC (C2), and MgO (C3); and (b) the decomposition of HM-20$NaNO_3$ with components assigned to HM-20$NaNO_3$ (C1), AMC-20$NaNO_3$ (C2), crystalline-$MgCO_3$-20$NaNO_3$ (C3), and MgO-20$NaNO_3$ (C4). The green vertical area in Fig. 4b corresponds to the meting point of $NaNO_3$ while grey vertical areas in Fig. 4a and b correspond to isothermal conditions. The lack of data fit (LOF) and the standard deviation were 2.2 and 1.7% and 9.6×10^{-3} and 7.6×10^{-3} for HM and HM-20$NaNO_3$, respectively.

from MCR-ALS analysis are ascribed to: C1 = HM-20$NaNO_3$, C2 = AMC-20$NaNO_3$, C3 = crystalline-$MgCO_3$-20$NaNO_3$ and C4 = MgO-20$NaNO_3$. Hence, the thermal decomposition of HM-20$NaNO_3$ proceeds *via* the intermediates AMC and crystalline-$MgCO_3$, yielding ultimately MgO mixed with molten $NaNO_3$. It should be noted that MCR-ALS analysis did not provide information on the $NaNO_3$ phase transition, possibly due to the highly overlapping signal in the PDF and the relatively low content of $NaNO_3$ with respect to HM. However, the XRD data showed that the melting of $NaNO_3$ occurred between 305 °C and 308 °C (Fig. S4 and S11†). The structural changes of $NaNO_3$ are visualized in Fig. 2. The temporal evolution of these four components is shown in Fig. 4b. In the first stage of the release of water of crystallization, the formation of AMC takes place. Subsequently, at *ca.* 305 °C, AMC converted rapidly to crystalline-$MgCO_3$ upon melting of $NaNO_3$. The formation of crystalline $MgCO_3$ was facilitated by the rapid release of H_2O from the structure upon melting of the salt, as observed in Fig. 1d, that acts as a phase-transfer agent. MgO started to form at 305 °C, in parallel to the formation of crystalline-$MgCO_3$, which decomposed fully to MgO at *ca.* 410 °C.

In summary, the PDF/XRD results show that crystalline MgO formed from HM-20$NaNO_3$ through the AMC and crystalline $MgCO_3$ intermediates. This is in contrast to the thermal decomposition of HM, which proceeds through AMC only. The presence of molten $NaNO_3$ accelerated the release of both H_2O (from water of crystallization and through dehydroxylation) and CO_2, affecting not only the decomposition pathways, but also promoting the crystallization of MgO at lower temperatures compared to HM.

Structural characterization of the produced MgO. After the decomposition of HM and HM-20$NaNO_3$, *i.e.*, their complete transformation to MgO ($HM_{(MgO\text{-}308)}$ and HM-20$NaNO_{3(MgO\text{-}308)}$), the samples were cooled down to 308 °C (a typical carbonation temperature of MgO) and analysed by XRD and PDF. For both cases, the MgO obtained exhibited a periclase structure (XRD analysis shown in Fig. S18†) with average crystallite sizes of *ca.* 3.8 and *ca.* 10.7 nm, respectively, as determined by peak broadening analysis implemented in the Rietveld refinement of the XRD data, (Tables S4–S6†). The larger average crystallite size of HM-20$NaNO_{3(MgO\text{-}308)}$ confirmed that molten $NaNO_3$ induced crystal growth of MgO. The line profile analysis also allowed us to determine the average lattice microstrain; values of 0.62% and 0.24% were determined for $HM_{(MgO\text{-}308)}$ and HM-20$NaNO_{3(MgO\text{-}308)}$, respectively. The higher lattice microstrain in $HM_{(MgO\text{-}308)}$ is probably due to its smaller crystallite size and suggests a more disordered nature of this material.[61] The cell parameters of MgO refined by the Rietveld method (Fig. S18†), showed that HM-20$NaNO_{3(MgO\text{-}308)}$ exhibited a slightly smaller cell parameter of 4.224(1) Å, compared to the refined value for $HM_{(MgO\text{-}308)}$ of 4.229(4) Å (Table 1). It is worth noting that these cell parameters indicate that Na^+ ions were not incorporated into the lattice of MgO. If this would have been the case, we would have expected a lattice expansion of MgO for HM-20$NaNO_{3(MgO\text{-}308)}$ with respect to $HM_{(MgO\text{-}308)}$ due to the larger Shannon effective ionic radius of Na^+ (1.02 Å) compared to Mg^{2+} (0.72 Å).[62,63]

Table 1 Structural parameters of $HM_{(MgO\text{-}308)}$ and HM-20$NaNO_{3(MgO\text{-}308)}$ determined by the Rietveld refinement of the XRD data

Material	Average crystallite size, nm	Cell parameter *a*, Å	*U*, Å^2
$HM_{(MgO\text{-}308)}$	3.8	4.229(4)	0.020(1)
HM-20$NaNO_{3(MgO\text{-}308)}$	10.7	4.224(1)	0.016(1)

The slightly larger unit cell parameter observed for $HM_{(MgO\text{-}308)}$ with respect to HM-20$NaNO_{3(MgO\text{-}308)}$ was likely due to the smaller crystallite size of $HM_{(MgO\text{-}308)}$.[64–66] A higher degree of structural disorder in $HM_{(MgO\text{-}308)}$ compared to HM-20$NaNO_{3(MgO\text{-}308)}$ is also evidenced by larger refined atomic displacement parameters (*U* in Tables 1 and 2). The results of PDF data fitting are in line with the XRD analysis, exhibiting the same trends in crystallite sizes, cell parameter and structural disorder (Table 2, Fig. S19 and S21†). However, slightly smaller values of the crystallite sizes were obtained by PDF analysis when compared to the values obtained by XRD, possibly due to the different influence of the instrumental resolution on the peak broadening. Nonetheless, it should be noted that the values determined by the two different analyses represent an estimation of the average crystallite size, and a distribution of sizes and shapes can also be expected (further discussion about particle shape will be inferred based on HAADF-STEM, *vide infra*). Comparison of the PDFs of the samples revealed that the peaks were sharper and more well-defined for HM-20$NaNO_{3(MgO\text{-}308)}$ than $HM_{(MgO\text{-}308)}$ (Fig. S19†). The width of the PDF peaks provides information about the static and dynamic disorder of the atoms involved in the atomic correlations.[67] This is reflected by the larger ADPs of the PDF data (Table 2, Fig. S21†) for $HM_{(MgO\text{-}308)}$ compared to HM-20$NaNO_{3(MgO\text{-}308)}$. In addition, the Mg–O peak in $HM_{(MgO\text{-}308)}$ shows a higher asymmetry (Fig. S19b and S21c, d†) which suggests that a distorted Mg–O local environment remains in $HM_{(MgO\text{-}308)}$. This remaining distortion may arise from disordered regions at the surface of the nanoparticles. This is in line with Rietveld refinement and can be attributed to an increased structural disorder of $HM_{(MgO\text{-}308)}$ due to the smaller size of its MgO crystallites. Additionally, the dampening of the PDF oscillations at high *r* relates to the finite size effect of the MgO particles, *i.e.*, the smaller the crystallites, the shorter the *r* at which the PDF peaks decays to zero.[68] We observed a more pronounced dampening of correlations in $HM_{(MgO\text{-}308)}$ than in HM-20$NaNO_{3(MgO\text{-}308)}$, indicative of a

Table 2 Structural parameters of $HM_{(MgO\text{-}308)}$ and HM-20$NaNO_{3(MgO\text{-}308)}$ determined by fitting of PDF data

Material	Crystallite size diameter, nm	Cell parameter *a*, Å	U_{iso}(O), Å^2	U_{iso}(Mg), Å^2
$HM_{(MgO\text{-}308)}$	3.5(2)	4.231(3)	0.014(2)	0.010(1)
HM-20$NaNO_{3(MgO\text{-}308)}$	10(2)	4.220(2)	0.012(1)	0.009(1)

smaller coherence length (*i.e.*, a smaller crystallite size) of the MgO in $HM_{(MgO\text{-}308)}$.

***In situ* determination of the CO_2 capture performance of the produced materials.** Besides thermal decomposition, also the carbonation behaviour of $HM_{(MgO\text{-}308)}$ and $HM\text{-}20NaNO_{3(MgO\text{-}308)}$ was studied by PDF analysis (Fig. S22†), to assess their CO_2 capture capacity.[11] The phase evolution of the materials under carbonation conditions was analysed using linear combination fitting (LCF) analysis, using MgO and $MgCO_3$ as references materials (more details can be found in the ESI†). In the case of $HM_{(MgO\text{-}308)}$, after 7 min of carbonation, 3 wt% of $MgCO_3$ is formed, reaching however, rapidly a conversion plateau. After 30 min of carbonation only 4 wt% $MgCO_3$ is present. On the other hand, for $HM\text{-}20NaNO_{3(MgO\text{-}308)}$ 80 wt% of $MgCO_3$ is obtained after 30 min of carbonation, confirming the promotion of the carbonation by molten $NaNO_3$ (Fig. S23†), in line with previous reports.[11,69–71] Moreover, these results show that PDF can provide quantitative information about the rate of carbonation in MgO-based sorbents.

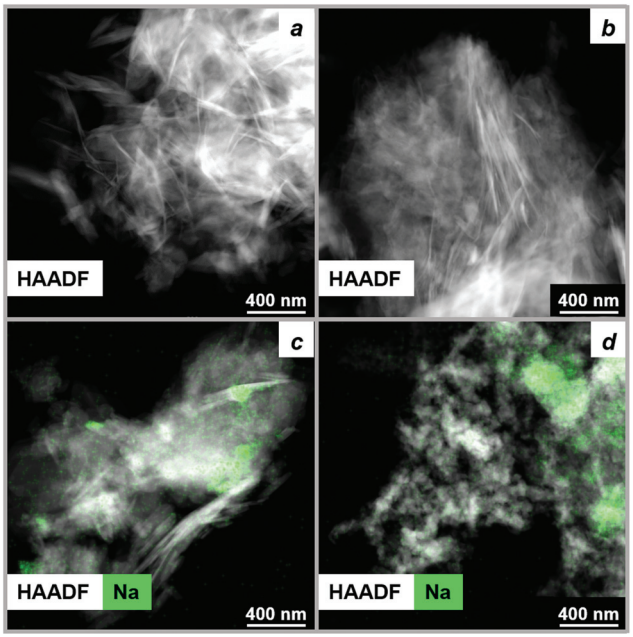

Fig. 5 HAADF-STEM images along with Na EDX maps of (a) as-received HM, (b) HM after thermal treatment in N_2 at 450 °C, (c) as-prepared $HM\text{-}20NaNO_3$ and (d) $HM\text{-}20NaNO_3$ after thermal treatment in N_2 at 450 °C.

Morphological characterization of the produced MgO by electron microscopy

To compare the morphology of the final MgO particles and initial precursor at a submicron scale, *ex situ* HAADF-STEM method was used. HAADF-STEM images of HM and $HM\text{-}20NaNO_3$ prior to and after their thermal decomposition at 450 °C (N_2, 10 °C min^{-1} performed in a TGA) are shown in Fig. 5 and the corresponding TEM images in Fig. S24.† MgO particles obtained from HM retained the plate-like morphology of HM (Fig. 5a and b) which is likely related to their transformation through an amorphous intermediate with a gradual release of water of crystallization and dehydroxylation. On the other hand, the morphology of MgO produced from $HM\text{-}20NaNO_3$ was considerably different from that of HM in

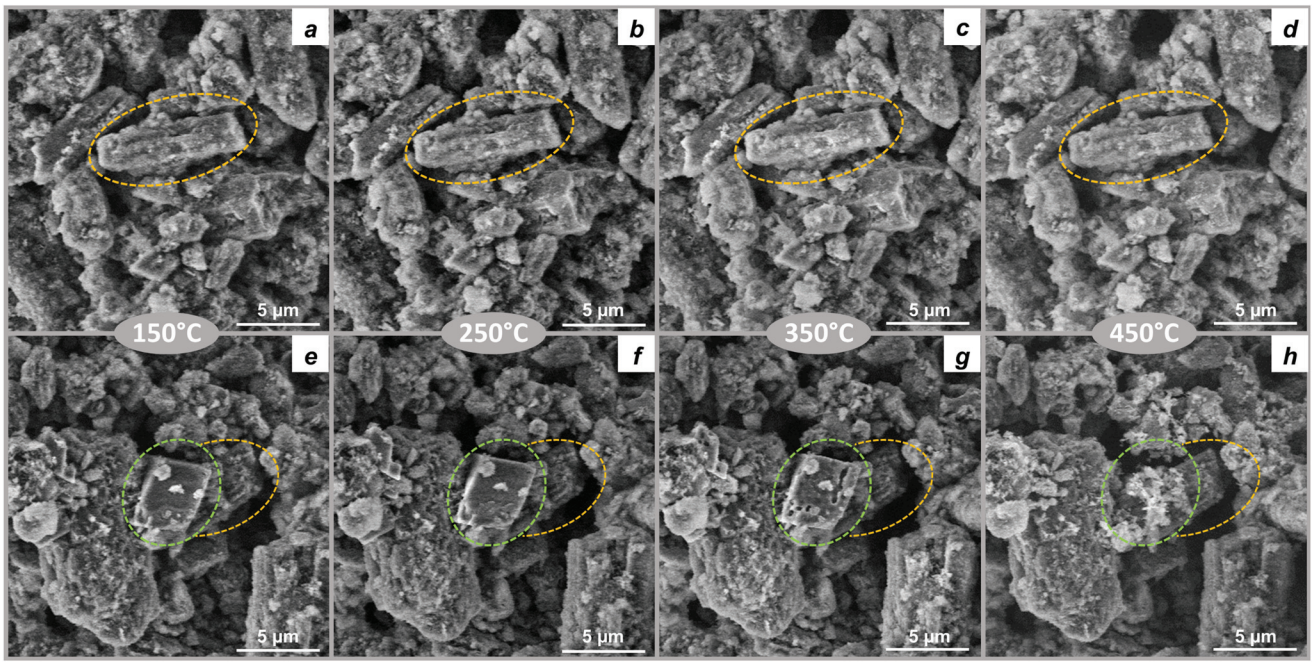

Fig. 6 *In situ* SEM images obtained while heating (a–d) HM and (e–h) $HM\text{-}20NaNO_3$ from 100 °C to 450 °C in 46 Pa of N_2. The areas highlighted in yellow in Fig. 6a–h shows the HM particle agglomerates, while areas highlighted in green in Fig. 6e–h emphasizes the thermal evolution of typical $NaNO_3$ particle.

terms of size and shape of the MgO particles. MgO particles of irregular shape (10–80 nm) and aggregates were formed from HM-20$NaNO_3$ (Fig. 5c and d and Fig. S24†).

The surface area of decomposed HM-20$NaNO_3$ is significantly lower than that of decomposed HM (33 and 306 $m^2\ g^{-1}$ respectively, according to N_2 physisorption, Table S7†). We attribute the morphological differences of MgO produced from HM and HM-20$NaNO_3$ to their transitioning through different intermediates, as determined by MCR-ALS analysis. Previous studies have also shown that the decomposition pathway of the precursors strongly determines the final MgO morphology.[40,63,72,73]

Visualization of MgO formation from HM by *in situ* SEM

In situ SEM allowed us to visualize the evolution of HM and HM-20$NaNO_3$ precursors at the micron scale during their thermal decomposition in N_2 between 150 and 450 °C (46 Pa, 10 °C min^{-1}, Fig. 6 and Movie S1†). HM exhibits the typical plate-like morphology forming larger agglomerates with sizes of several microns. The morphology of HM does not change significantly with heating up to 450 °C, confirming the continuous nature of the HM decomposition (Fig. 6a–d). In HM-20$NaNO_3$, $NaNO_3$ particles with polyhedral shape can be identified (marked as a green area in Fig. 6, panels e-h and also visible in Movie S1†) among HM particles. The shrinkage of HM particles is observed at 200 °C and is likely related to the release of water of crystallization as indicated by TGA results discussed above. $NaNO_3$ starts to melt at *ca.* 300 °C and this process is associated with a formation of cavities and channels at the surface of the $NaNO_3$ particles. Close to 400 °C, $NaNO_3$ particles are no longer observed by *in situ* SEM, explained by their melting. The melting of $NaNO_3$ affects the morphology of the nearby HM particles, which we interpret as the formation of MgO in the proximity of molten $NaNO_3$ (in correlation with TGA and PDF studies). The change is rather sudden, which is in line with the promoted formation of MgO in the presence of molten $NaNO_3$ (Movie S1†).

Conclusions

TGA and HF coupled with gas analysis showed that molten $NaNO_3$ accelerated the decomposition of HM through the dehydration, dehydroxylation and decarbonation steps. In the presence of $NaNO_3$, the temperature for the complete conversion of HM to MgO was lowered by *ca.* 100 °C. The PDF analysis of *in situ* total scattering data, complemented by MCR-ALS analysis, demonstrated that the presence of molten $NaNO_3$ has a crucial influence on the decomposition pathways of HM and the structure of the resulting MgO. In the case of pristine HM, the decomposition occurred through an amorphous intermediate that formed upon the release of water of crystallization. Importantly, the amorphization process was accompanied by a rearrangement of the local structure resulting in the splitting of the Mg–O correlation. The Mg–O splitting intensified upon dehydroxylation at higher temperatures. Below the melting point of $NaNO_3$, the decomposition of the promoted sample occurred in a similar fashion as for pristine HM and an amorphous intermediate was formed. However, melting of $NaNO_3$ induces a rapid crystallization of the amorphous intermediate into crystalline $MgCO_3$ and MgO, which was followed by the rapid decomposition of $MgCO_3$ to MgO. MCR-ALS analysis further confirmed the lowering of the decomposition temperature of promoted HM by *ca.* 100 °C.

Concerning the structure and morphology of the MgO formed, the presence of $NaNO_3$ led to an increase of its average crystallite size reaching approximately 10.7 nm, whereas the pristine sample yielded MgO with an average crystallite size of 3.8 nm only, and with a higher degree of structural disorder. The larger average crystallite size is in line with the morphological differences of MgO observed *via ex situ* HAADF-STEM, showing the formation of highly crystalline nanoparticles in the presence of $NaNO_3$. *In situ* SEM allowed to visualize the morphological changes occurring in HM promoted with $NaNO_3$, at the micrometre scale.

We expect that the obtained atomic level insights on the effect of molten $NaNO_3$ on the decomposition pathways of HM and the morphology and properties of the resultant MgO will aid the design of improved MgO-based sorbents and set the basis for further investigations of the mechanism of $MgCO_3$ formation and growth. Improving the performance of MgO-based CO_2 sorbents will rely critically on the rational selection of the most appropriate promoter. On the other hand, optimization of the surface area and crystallite size of MgO do not seem to be the prime parameters to optimize the CO_2 capture performance of the sorbent. The presence of a promoter is a pre-requisite for MgO to act as a practical CO_2 sorbent, therefore, determining the exact role of the promoter in carbonation and calcination reactions is key for the manufacture of more effective sorbents. Additionally, we have showcased the potential of PDF analysis for materials research on CO_2 sorbents. Forthcoming studies shall shed light onto the growth of $MgCO_3$ and the nature of the interaction between MgO and $NaNO_3$ at the interface by surface sensitive techniques.

Conflicts of interest

There are no conflicts to declare.

Acknowledgements

This project has received funding from the European Research Council (ERC) under the European Union's Horizon 2020 research and innovation programme grant agreement No. 819573 and from Swiss National Science Foundation (SNSF, 200020_156015). The SNSF Project 206021_183290 "Multi-Scale *in situ* observation of functional materials in their relevant state" is acknowledged. We thank the Scientific Centre for Optical and Electron Microscopy (ScopeM) for providing training on and access to electron microscopes. The ESRF is acknowledged for providing access to beam-time through pro-

posal MA-3415. P. M. Abdala would like to acknowledge the ETH SEED grant scheme (SEED-02 17-2) and J. Drnec is acknowledged for his assistance during total scattering measurements.

Notes and references

1 J.-M. Barnola, D. Raynaud, Y. S. Korotkevich and C. Lorius, *Nature*, 1987, **329**, 408–414.
2 Trends in Atmospheric Carbon Dioxide, https://www.esrl.noaa.gov/gmd/ccgg/trends, (accessed January 2020).
3 B. D. Santer, K. Taylor, T. Wigley, T. Johns, P. Jones, D. Karoly, J. Mitchell, A. Oort, J. Penner and V. Ramaswamy, *Nature*, 1996, **382**, 39–46.
4 International Energy Agency, *CO2 emissions from fuel combustion – Highlights*, IEA Publications, Paris, 2017.
5 A. Hassanzadeh and J. Abbasian, *Fuel*, 2010, **89**, 1287–1297.
6 X. Zhao, G. Ji, W. Liu, X. He, E. J. Anthony and M. Zhao, *Chem. Eng. J.*, 2018, **332**, 216–226.
7 J. Chi, L. Zhao, B. Wang, Z. Li, Y. Xiao and Y. Duan, *Int. J. Hydrogen Energy*, 2014, **39**, 6479–6491.
8 F. Goff and K. Lackner, *Environ. Geosci.*, 1998, **5**, 89–101.
9 W. Gao, L. Sun and Q. Wang, in *Pre-combustion Carbon Dioxide Capture Materials*, ed. Q. Wang, The Royal Society of Chemistry, Cambridge, 2018, ch. 2, pp. 61–143.
10 Y. Qiao, J. Wang, Y. Zhang, W. Gao, T. Harada, L. Huang, T. A. Hatton and Q. Wang, *Ind. Eng. Chem. Res.*, 2017, **56**, 1509–1517.
11 A. Dal Pozzo, A. Armutlulu, M. Rekhtina, P. M. Abdala and C. R. Müller, *ACS Appl. Energy Mater.*, 2019, **2**, 1295–1307.
12 Y. Hu, Y. Guo, J. Sun, H. Li and W. Liu, *J. Mater. Chem. A*, 2019, **7**, 20103–20120.
13 X. Yang, L. Zhao, Y. Liu, Z. Sun and Y. Xiao, *Ind. Eng. Chem. Res.*, 2016, **56**, 342–350.
14 M. L. T. Triviño, V. Hiremath and J. G. Seo, *Environ. Sci. Technol.*, 2018, **52**, 11952–11959.
15 A.-T. Vu, Y. Park, P. R. Jeon and C.-H. Lee, *Chem. Eng. J.*, 2014, **258**, 254–264.
16 K. Zhang, X. S. Li, W. Z. Li, A. Rohatgi, Y. Duan, P. Singh, L. Li and D. L. King, *Adv. Mater. Interfaces*, 2014, **1**, 1400030.
17 T. Harada, F. Simeon, E. Z. Hamad and T. A. Hatton, *Chem. Mater.*, 2015, **27**, 1943–1949.
18 H. Lee, M. L. T. Triviño, S. Hwang, S. H. Kwon, S. G. Lee, J. H. Moon, J. Yoo and J. G. Seo, *ACS Appl. Mater. Interfaces*, 2018, **10**, 2414–2422.
19 S.-I. Jo, Y.-I. An, K.-Y. Kim, S.-Y. Choi, J.-S. Kwak, K.-R. Oh and Y.-U. Kwon, *Phys. Chem. Chem. Phys.*, 2017, **19**, 6224–6232.
20 Hydromagnesite, http://www.handbookofmineralogy.org/pdfs/hydromagnesite.pdf, (accessed January 2020).
21 S. Jin, K. Ho, A.-T. Vu and C.-H. Lee, *Energy Fuels*, 2017, **31**, 9725–9735.
22 Y. Sawada, K. Uematsu, N. Mizutani and M. Kato, *Thermochim. Acta*, 1978, **27**, 45–59.
23 D. Bhattacharjya, T. Selvamani and I. Mukhopadhyay, *J. Therm. Anal. Calorim.*, 2012, **107**, 439–445.
24 C. Janet, B. Viswanathan, R. Viswanath and T. Varadarajan, *J. Phys. Chem. C*, 2007, **111**, 10267–10272.
25 N. Koga and Y. Yamane, *J. Therm. Anal. Calorim.*, 2008, **93**, 963–971.
26 L. Hollingbery and T. Hull, *Thermochim. Acta*, 2010, **509**, 1–11.
27 P. Ballirano, C. De Vito, S. Mignardi and V. Ferrini, *Chem. Geol.*, 2013, **340**, 59–67.
28 S. J. Billinge and M. G. Kanatzidis, *Chem. Commun.*, 2004, **7**, 749–760.
29 C. E. White, N. J. Henson, L. L. Daemen, M. Hartl and K. Page, *Chem. Mater.*, 2014, **26**, 2693–2702.
30 M. Albéric, L. Bertinetti, Z. Zou, P. Fratzl, W. Habraken and Y. Politi, *Adv. Sci.*, 2018, **5**, 1701000.
31 A. E. Morandeau and C. E. White, *J. Mater. Chem. A*, 2015, **3**, 8597–8605.
32 A. Van der Eerden, J. A. van Bokhoven, A. Smith and D. Koningsberger, *Rev. Sci. Instrum.*, 2000, **71**, 3260–3266.
33 J. Xto, R. Wetter, C. N. Borca, C. Frieh, J. A. van Bokhoven and T. Huthwelker, *RSC Adv.*, 2019, **9**, 34004–34010.
34 W. van Beek, O. V. Safonova, G. Wiker and H. Emerich, *Phase Transitions*, 2011, **84**, 726–732.
35 J. Kieffer and D. Karkoulis, *J. Phys.: Conf. Ser.*, 2013, **425**, 202012.
36 P. Juhás, T. Davis, C. L. Farrow and S. J. Billinge, *J. Appl. Crystallogr.*, 2013, **46**, 560–566.
37 C. Farrow, P. Juhas, J. Liu, D. Bryndin, E. Božin, J. Bloch, T. Proffen and S. Billinge, *J. Phys.: Condens. Matter*, 2007, **19**, 335219.
38 J. Rodriguez-Carvajal and T. Roisnel, *IUCrJ*, 1998, **20**, 35–36.
39 J. Jaumot, A. de Juan and R. Tauler, *Chemom. Intell. Lab. Syst.*, 2015, **140**, 1–12.
40 A. Shkatulov, T. Krieger, V. Zaikovskii, Y. Chesalov and Y. Aristov, *ACS Appl. Mater. Interfaces*, 2014, **6**, 19966–19977.
41 P. Ballirano, *Phys. Chem. Miner.*, 2011, **38**, 531–541.
42 S. Antao, I. Hassan, W. Mulder and P. Lee, *Phys. Chem. Miner.*, 2008, **35**, 545–557.
43 W. Gonschorek, W. W. Schmahl, H. Weitzel, G. Miehe and H. Fuess, *Z. Kristallogr.*, 1995, **210**, 843–849.
44 W. W. Schmahl and E. Salje, *Phys. Chem. Miner.*, 1989, **16**, 790–798.
45 S. Tahara, H. Toyama, H. Shimakura and T. Fukami, *EPJ Web Conf.*, 2017, **151**, 01004.
46 H. Ohno and K. Furukawa, *J. Chem. Soc., Faraday Trans. 1*, 1978, **74**, 1861–1870.
47 M. C. Wilding, M. Wilson, M. C. Ribeiro, C. J. Benmore, J. Weber, O. Alderman, A. Tamalonis and J. Parise, *Phys. Chem. Chem. Phys.*, 2017, **19**, 21625–21638.
48 M. Akao and S. Iwai, *Acta Crystallogr., Sect. B: Struct. Crystallogr. Cryst. Chem.*, 1977, **33**, 1273–1275.
49 M. Akao, F. Marumo and S. Iwai, *Acta Crystallogr., Sect. B: Struct. Crystallogr. Cryst. Chem.*, 1974, **30**, 2670–2672.

50 S. Bach, E. Visnow, M. Panthöfer, T. Gorelik, A. G. Buzanich, A. Gurlo, U. Kolb, F. Emmerling, C. Lind and W. Tremel, *Eur. J. Inorg. Chem.*, 2016, **2016**, 2072–2081.
51 A. C. Jensen, S. Imberti, S. F. Parker, E. Schneck, Y. Politi, P. Fratzl, L. Bertinetti and W. J. Habraken, *J. Phys. Chem. C*, 2018, **122**, 3591–3598.
52 H. Du and E. Amstad, *Angew. Chem., Int. Ed.*, 2020, **59**, 1798–1816.
53 X. Qiu, E. S. Božin, P. Juhas, T. Proffen and S. J. Billinge, *J. Appl. Crystallogr.*, 2004, **37**, 110–116.
54 M. Khanmohammadi, S. Amani and A. B. Garmarudi, *Anal. Methods*, 2016, **8**, 2799–2804.
55 J. P. Smith, E. C. Holahan, F. C. Smith, V. Marrero and K. S. Booksh, *Analyst*, 2019, **144**, 5425–5438.
56 A. Tsoukalou, P. M. Abdala, D. Stoian, X. Huang, M.-G. Willinger, A. Fedorov and C. R. Müller, *J. Am. Chem. Soc.*, 2019, **141**, 13497–13505.
57 A. Taris, M. Grosso, M. Brundu, V. Guida and A. Viani, *J. Appl. Crystallogr.*, 2017, **50**, 451–461.
58 M. Roelsgaard, A.-C. Dippel, K. A. Borup, I. G. Nielsen, N. L. N. Broge, J. T. Röh, O. Gutowski and B. B. Iversen, *IUCrJ*, 2019, **6**, 299–304.
59 F. M. Michel, V. Barrón, J. Torrent, M. P. Morales, C. J. Serna, J.-F. Boily, Q. Liu, A. Ambrosini, A. C. Cismasu and G. E. Brown, *Proc. Natl. Acad. Sci. U. S. A.*, 2010, **107**, 2787–2792.
60 J. Jaumot, R. Gargallo, A. de Juan and R. Tauler, *Chemom. Intell. Lab. Syst.*, 2005, **76**, 101–110.
61 S. Y. Yao, W. Q. Xu, A. C. Johnston-Peck, F. Z. Zhao, Z. Y. Liu, S. Luo, S. D. Senanayake, A. Martínez-Arias, W. J. Liu and J. A. Rodriguez, *Phys. Chem. Chem. Phys.*, 2014, **16**, 17183–17195.
62 R. D. Shannon, *Acta Crystallogr., Sect. A: Cryst. Phys., Diffr., Theor. Gen. Crystallogr.*, 1976, **32**, 751–767.
63 J. Green, *J. Mater. Sci.*, 1983, **18**, 637–651.
64 A. Cimino, P. Porta and M. Valigi, *J. Am. Ceram. Soc.*, 1966, **49**, 152–156.
65 P. M. Diehm, P. Ágoston and K. Albe, *ChemPhysChem*, 2012, **13**, 2443–2454.
66 B. M. Maoz, E. Tirosh, M. B. Sadan, I. Popov, Y. Rosenberg and G. Markovich, *J. Mater. Chem.*, 2011, **21**, 9532–9537.
67 A. S. Masadeh, *J. Exp. Nanosci.*, 2016, **11**, 951–974.
68 V. Petkov, in *Characterization of Materials*, ed. E. N. Kaufmann, Wiley, New York, 2012, pp. 1361–1372.
69 H. Cui, Q.-M. Zhang, Y. Hu, C. Peng, X. Fang, Z.-M. Cheng, V. V. Galvita and Z. Zhou, *ACS Appl. Mater. Interfaces*, 2018, **10**, 20611–20620.
70 K. Zhang, X. S. Li, H. Chen, P. Singh and D. L. King, *J. Phys. Chem. C*, 2015, **120**, 1089–1096.
71 T. Harada and T. A. Hatton, *Chem. Mater.*, 2015, **27**, 8153–8161.
72 M. D. Susman, H. N. Pham, A. K. Datye, S. Chinta and J. D. Rimer, *Chem. Mater.*, 2018, **30**, 2641–2650.
73 T. Xu, X. Zhou, Z. Jiang, Q. Kuang, Z. Xie and L. Zheng, *Cryst. Growth Des.*, 2008, **9**, 192–196.